The Astrophysical Journal, 753:47 (15pp), 2012 July 1 doi:10.1088/0004-637X/753/1/47
© 2012. The American Astronomical Society. All rights reserved. Printed in the U.S.A.

A *CHANDRA*–VLA INVESTIGATION OF THE X-RAY CAVITY SYSTEM AND RADIO MINI-HALO IN THE GALAXY CLUSTER RBS 797

Alberto Doria[1], Myriam Gitti[2,3,4], Stefano Ettori[3], Fabrizio Brighenti[2], Paul E. J. Nulsen[5], and Brian R. McNamara[5,6,7]
[1] Argelander-Institut für Astronomie, Auf dem Hügel 71, D-53121 Bonn, Germany
[2] Dipartimento di Astronomia, Università di Bologna, via Ranzani 1, Bologna 40127, Italy
[3] Astronomical Observatory of Bologna-INAF, via Ranzani 1, I-40127 Bologna, Italy
[4] Institute of Radioastronomy-INAF, via Gobetti 101, I-40129 Bologna, Italy
[5] Harvard-Smithsonian Center for Astrophysics, 60 Garden Street, Cambridge, MA 02138, USA
[6] Department of Physics & Astronomy, University of Waterloo, 200 University Avenue West, Waterloo, Ontario, N2L 2G1, Canada
[7] Perimeter Institute for Theoretical Physics, Waterloo, Canada
Received 2012 February 7; accepted 2012 April 26; published 2012 June 13

ABSTRACT

We present a study of the cavity system in the galaxy cluster RBS 797 based on *Chandra* and Very Large Array (VLA) data. RBS 797 ($z = 0.35$) is one of the most distant galaxy clusters in which two pronounced X-ray cavities have been discovered. The *Chandra* data confirm the presence of a cool core and indicate a higher metallicity along the cavity directions. This is likely due to the active galactic nucleus outburst, which lifts cool metal-rich gas from the center along the cavities, as seen in other systems. We find indications that the cavities are hotter than the surrounding gas. Moreover, the new *Chandra* images show bright rims contrasting with the deep, X-ray deficient cavities. The likely cause is that the expanding 1.4 GHz radio lobes have displaced the gas, compressing it into a shell that appears as bright cool arms. Finally, we show that the large-scale radio emission detected with our VLA observations may be classified as a radio mini-halo, powered by the cooling flow, as it nicely follows the trend $P_{\rm radio}$ versus $P_{\rm CF}$ predicted by the reacceleration model.

Key words: galaxies: active – galaxies: clusters: individual (RBS 797) – galaxies: clusters: intracluster medium – galaxies: jets – radio continuum: galaxies – X-rays: galaxies: clusters

Online-only material: color figures

1. INTRODUCTION

Imaging spectroscopy obtained with the new generation of X-ray telescopes indicates that the spectra of clusters of galaxies with "cool cores" show no evidence of any cooler phase of the intracluster medium (ICM) below an intermediate temperature of ∼1–2 keV. In particular, it has also been found that line emission from gas with $kT < 1$ keV was either lacking in the spectra of cool core clusters or was weaker than expected (Peterson et al. 2001; Tamura et al. 2001). Many possible explanations of this "cooling flow (CF) problem" have been suggested in the past decade, like differential absorption, thermal conduction, intracluster supernovae, subcluster merging, or inhomogeneous metallicity distributions (e.g., see Peterson & Fabian 2006 for a review).

Heating by a central active galactic nucleus (AGN) in galaxy clusters has become the most credible scenario to explain the CF problem (for recent reviews, see Gitti et al. 2012; McNamara & Nulsen 2007 and references therein). In this scenario, the central cD galaxies of clusters drive strong jet outflows which interact with the hot plasma of the ICM, inflating lobes of radio-synchrotron emission. As a consequence, the gas is displaced, forming X-ray deficient regions, which are thus called "cavities." It is believed that such peculiar features can heat the cluster gas in various ways. Furthermore, the cavities are often filled with relativistic particles and magnetic fields, as indicated by the observation of radio lobes spatially coincident with the X-ray cavities (e.g., Gitti et al. 2012; McNamara & Nulsen 2007).

Studies of individual clusters confirm a strong interplay between the ICM and the radio sources in their cores, e.g., Perseus (Böhringer et al. 1993; Churazov et al. 2000; Fabian et al. 2000, 2006), A2052 (Blanton et al. 2001, 2009, 2011), MS0735.6+7421 (McNamara et al. 2005; Gitti et al. 2007a), and Hydra A (McNamara et al. 2000; Nulsen et al. 2005; Wise et al. 2007; Simionescu et al. 2009a; Gitti et al. 2011). Nevertheless, the X-ray luminous, relatively distant galaxy cluster RBS 797 ($z = 0.35$) seems to be one of the most striking examples of this interaction.

RBS 797 was detected for the first time in the ROSAT All-Sky Survey (RASS; Schwope et al. 2000) as the X-ray source RXS J094713.2+762317, and was observed in the optical band by the ROSAT Bright Survey (RBS) during the optical identification of all bright (count rate >0.2 counts s^{-1}), high-galactic latitude ($|b| > 30°$) X-ray sources found in the RASS (Fischer et al. 1998; Schwope et al. 2000). Early observations with *Chandra* revealed two pronounced X-ray minima, which are located on opposite sides of the cluster center (Schindler et al. 2001) and represent a striking example of a cavity system in a galaxy cluster. A recent, deeper *Chandra* image has confirmed the presence of the cavity system, allowing a more detailed study. By considering a complex cavity configuration extended along our line of sight, Cavagnolo et al. (2011) provide new estimates of the energy of the central AGN outburst (up to 6×10^{60} erg) and of the jet power (up to 6×10^{45} erg s^{-1}). Furthermore, Cavagnolo et al. (2011) show that the AGN of RBS 797 must be powered principally by accretion of cold gas, and that its powerful outburst might be due to the energy released by a maximally spinning black hole. Structures associated with star formation in the bright central galaxy have also been found thanks to new *Hubble Space Telescope* (Cavagnolo et al. 2011) images.

RBS 797 was observed at radio frequencies with the Very Large Array (VLA) in the years 2001–2004. With these

observations, performed at different frequencies and resolutions, it was possible to detect radio emission on three different scales and orientations, indicating that RBS 797 represents a very peculiar case (Gitti et al. 2006). In particular, the X-ray cavities were found to be filled with 1.4 GHz radio emission. Furthermore, diffuse radio emission was detected on a scale of hundreds of kpc, which is roughly comparable to the size of the cooling region. This extended radio emission is characterized by amorphous morphology and a steep spectrum that steepens with distance from the center. These characteristics point to a possible classification of the diffuse radio source as a mini-halo (Gitti et al. 2006).

In this paper, we present a new analysis of the recent, deeper *Chandra* X-ray data. We also present new VLA observations at 1.4 GHz that confirm the presence of large-scale radio emission. Based on our joint X-ray/radio analysis, we investigate the physical properties of the ICM and its interaction with the radio source, and discuss the possibility that RBS 797 hosts a diffuse radio mini-halo. In order to be consistent with the literature, we adopt the cosmology of a ΛCDM model by the following parameters: $H_0 = 70$ km s^{-1} Mpc^{-1}, and $\Omega_M = 1 - \Omega_\Lambda = 0.3$, the luminosity distance is 1858 Mpc and 1 arcsec corresponds to 4.8 kpc. Measurement uncertainties are 90% confidence levels unless stated otherwise.

2. OBSERVATIONS AND DATA REDUCTION

2.1. Chandra Data

RBS 797 was observed with the Chandra Advanced CCD Imaging Spectrometer I (ACIS-I) on 2000 October 20 (ObsID 2202), for a total exposure of 13.3 ks (Schindler et al. 2001). On 2007 July 9 (ObsID 7902), a new 38.3 ks was acquired with ACIS-S in imaging mode, operating at the focal plane temperature of −120° C. The two *Chandra* exposures were combined for our analysis, giving a total of 51.6 ks of uncleaned exposure time.

Data were reprocessed with CIAO 4.2, using CALDB 4.2.0 and corrected for known time-dependent gain problems following techniques similar to those described in the *Chandra* analysis threads.[8] Screening of the event files was applied to filter out strong background flares. Blank-sky background files, filtered in the same manner as in the RBS 797 image and normalized to the count rate of the source image in the 10–12 keV band, were used for background subtraction. The final exposure time is ∼49.6 ks.

For both chips, point sources have been identified and removed using the CIAO task `WAVDETECT`. The "holes" left by the discarded point sources are re-filled, for imaging purposes only, by values interpolated from surrounding background regions using the task `dmfilth`. Images, instrument maps, and exposure maps were created in the 0.5–7.0 keV band. Data with energies above 7.0 keV and below 0.5 keV were excluded in order to prevent background contamination and uncertainties in the ACIS calibration, respectively.

2.2. VLA Data

The existing VLA[9] data for the radio source RBS 797 at 300, 1400, 4800, and 8400 MHz have already been presented and discussed in Gitti et al. (2006), Bîrzan et al. (2008), and Cavagnolo et al. (2011). Here, we present new observations at 1.4 GHz performed in 2006 December with the VLA in C-array, a configuration that was not used in previous observations. The data were acquired in channels centered at 1465 and 1385 MHz, with a 50 MHz bandwidth, for a total integration time of 5 hr. In these observations, the source 3C 48 (0137+331) is used as the primary flux density calibrator, while the source 1044+809 is used as secondary phase calibrator. We have also performed a re-analysis of the archival 1.4 GHz data in A- and B-array, and then have added them together with the new 1.4 GHz data in C-array to produce a total, combined 1.4 GHz image.

Data reduction was done using the NRAO AIPS (Astronomical Image Processing System) package. Accurate editing of the UV data was applied to identify and remove bad data. Images were produced by following the standard procedures: Calibration, Fourier-Transform, Clean, and Restore. Self-calibration was applied to remove residual phase variations. The final images, produced using the AIPS task IMAGR, show the contours of the total intensity.

3. RESULTS

3.1. X-ray Morphology and Surface Brightness Profile

The pronounced central surface brightness peak (discussed below in this section) and the presence of strong O[II]λ3727 line, and weak, narrow Hβ and O[III]λλ4959/5007 emission lines (Schindler et al. 2001) indicate the presence of a central AGN recognized by Schindler et al. (2001). In order to avoid contamination by the central source, we exclude it in the spectral analysis (Section 4).

The raw ACIS-S image of RBS 797 in the 0.5–7 keV energy band is shown in the left panel of Figure 1. We confirm the presence of two central X-ray deficient lobes already discovered with the existing *Chandra* observations of RBS 797 (Schindler et al. 2001; Cavagnolo et al. 2011). These two striking features are ∼10 arcsec apart in an NE–SW orientation (Figure 1). The physical properties of the cavities are discussed in Section 6.1. The cavity system in RBS 797 is surrounded by bright rims. One possible explanation for the presence of these strong features is that the expansion of the 1.4 GHz radio lobes displaced the ICM formerly in the cavities, compressing it to form the bright rims that now surround the cavities (as seen in the right panel of Figure 1). In particular, the rims of the SW cavity appear to have a stronger contrast than the NE cavity rims, almost totally enclosing the SW cavity, while the NE rims seem to be more open and less bright. Beyond the cavities and rims, the cluster morphology is elliptical in shape.

These details are more evident in the *Chandra* unsharp masked image (Figure 1, right panel), which is created with an image reprocessing technique aimed at emphasizing possible substructures and faint features. We also note in the unsharp masked image that the cavity system appears to be surrounded by two edges, with the inner edge extending ∼8″–10″ from the core. An outer edge is also visible at ∼14″–17″. These features appear as edges in the surface brightness profile at ∼8″ and ∼20″ (see below). Taking into account these peculiarities, RBS 797 appears to be very similar to NGC 5813 (Randall et al. 2011), in which are observed distinct cavity systems due to multiple AGN outbursts. Also in RBS 797, as in NGC 5813, the edges seen in the *Chandra* X-ray image may be identified as weak shocks (for a further discussion about shocks see Section 3.3.3 in Cavagnolo et al. 2011). These shocks could be produced

[8] http://cxc.harvard.edu/ciao/threads/index.html

[9] The Very Large Array (VLA) is a facility of the National Radio Astronomy Observatory (NRAO). The NRAO is a facility of the National Science Foundation, operated under cooperative agreement by Associated Universities, Inc.

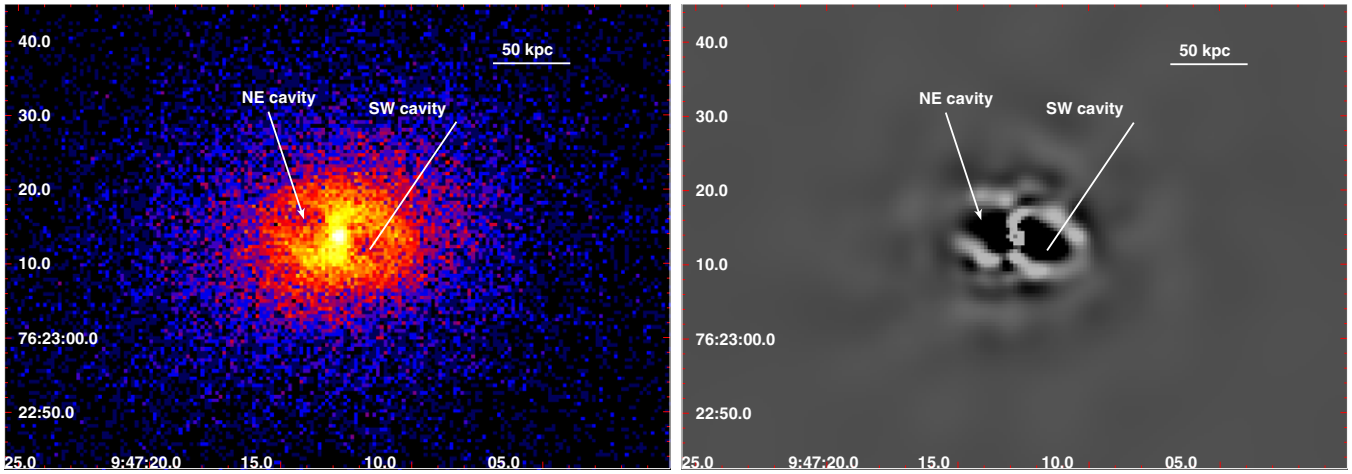

Figure 1. Raw (left panel) and unsharp masked (right panel) *Chandra* ACIS-S images of RBS 797 in the 0.5–7.0 keV energy band. The unsharp masked image is obtained by subtracting a strongly (S/N = 10) smoothed image from a lightly (S/N = 3) smoothed image. In these images and in all the following, north is up and east is left.

(A color version of this figure is available in the online journal.)

by distinct AGN outbursts, with the inner edge associated with the NE–SW inner cavities, and the outer edge associated with possible outer cavities.

We also performed a study of the surface brightness profile of RBS 797 by means of the *Chandra* ACIS-S data. An azimuthally averaged surface brightness profile was computed over the range 0.5–2.0 keV with the task `dmextract` by subtracting the background from the point-source-removed image and then dividing by the exposure map.

In particular, we considered 360° annular bins of 1″ width, starting from 2″ up to 150″. Since there is clear evidence of ICM/AGN interaction in the central region of RBS 797, we excluded the cavity system and the rims (see Figure 2) in order to get a profile of the so-called "undisturbed" ICM. This surface brightness profile was fitted with a single β-model (Cavaliere & Fusco-Femiano 1976) using the tool `SHERPA` with the χ^2 statistics with Gehrels' variance. A fit over the external 25″–110″ interval, which excludes the whole cooling region (green line in Figure 3), shows evidence of a central excess of the observed profile with respect to the β-model (Figure 3). This evident deviation from the fit prediction is a strong indication of the presence of a cool core in RBS 797, as seen in many other cool core clusters (Fabian 1994). We then fitted the surface brightness profile of the undisturbed cluster with a double β-model, finding that it is able to provide a better description of the entire profile ($\chi^2_{\rm red} \sim 0.96$ for 142 dof). The best-fit values for the double β-model (assuming a common β value) are core radii $r_c(1) = 3''.47 \pm 0''.28$ and $r_c(2) = 12''.89 \pm 1''.13$, central surface brightness $S_0(1) = 1.15 \pm 0.06 \times 10^{-6}$ and $S_0(2) = 2.21 \pm 0.50 \times 10^{-7}$, and slope parameters $\beta(1) = 0.6044 \pm 0.0543$ and $\beta(2) = 0.6332 \pm 0.0194$.

For a comparison of the surface brightness profile along the cavities with the azimuthally averaged profile, we considered two sectors along the cavity directions, chosen to be tangent to the cavities (Figure 2, in red). Figure 3 also shows the two profiles along the cavities compared separately with the azimuthally averaged profile. We found a clear drop in the radial range between 2″ and 7″ in both the surface brightness profiles along the cavities compared to the azimuthally averaged profile. These distances clearly correspond to the two X-ray deficient lobes, thus giving us a very good indication for the estimate of the cavity dimensions (see Section 6.1).

3.2. Radio Properties

RBS 797 is known to possess a unique radio source that exhibits large changes in orientation with scale. The subarcsec resolution radio image first presented by Gitti et al. (2006) shows the details of the innermost 4.8 GHz radio jets, which clearly point in a north–south direction. Remarkably, these inner jets are almost *perpendicular* to the axis of the 1.4 GHz emission detected at ∼1 arcsec resolution (A-array), which is elongated in the northeast–southwest direction, filling the X-ray cavities (see Figure 4 of Gitti et al. 2006). The ∼4 arcsec resolution VLA image at 1.4 GHz (B-array) shows large-scale radio emission with amorphous morphology, slightly extended in the north–south direction (see Figure 2 of Gitti et al. 2006).

Figure 4 (left panel) shows the radio map of RBS 797 observed at 1.4 GHz with the VLA in C-array configuration, with a restoring beam of $18''.3 \times 12''.2$. At this low resolution, the source is barely resolved, showing an amorphous morphology apparently extending to the north (an unrelated source is present to the east). The source has a total flux density of $\simeq 23.0 \pm 0.3$ mJy. In order to fully exploit the relative advantages in terms of angular resolution and sensitivity of the three VLA configurations used for the observations at 1.4 GHz, we have combined this new set of data taken with the C-array with the archival data from the A- and B-array. The total 1.4 GHz radio map, with a circular restoring beam of 3″, is shown in Figure 4 (right panel). This combined image is able to reveal the morphology of the radio source in the central ∼10 kpc, showing its elongation in the cavity direction, without losing flux at the larger scales. In particular, the radio emission is detected out to ∼90 kpc. The total flux density is $\simeq 24.0 \pm 0.3$ mJy.

In order to estimate the flux density of the diffuse radio emission, it is necessary to subtract the emission contributed by the central nuclear source. One way is to consider the high-resolution map. The central component imaged by the A-array observations (see Figure 2 of Gitti et al. 2006) is found to consist of a resolved core elongated in the northeast–southwest direction, plus a jet-like feature emanating from the center to the west. The total flux density coming from the central region (inner jets included) was measured by Gitti et al. (2006) as $\simeq 12.1 \pm 0.1$ mJy. Another way is to estimate the contribution of the central emission directly from the new combined image presented here (Figure 4, right panel). In this map, the flux

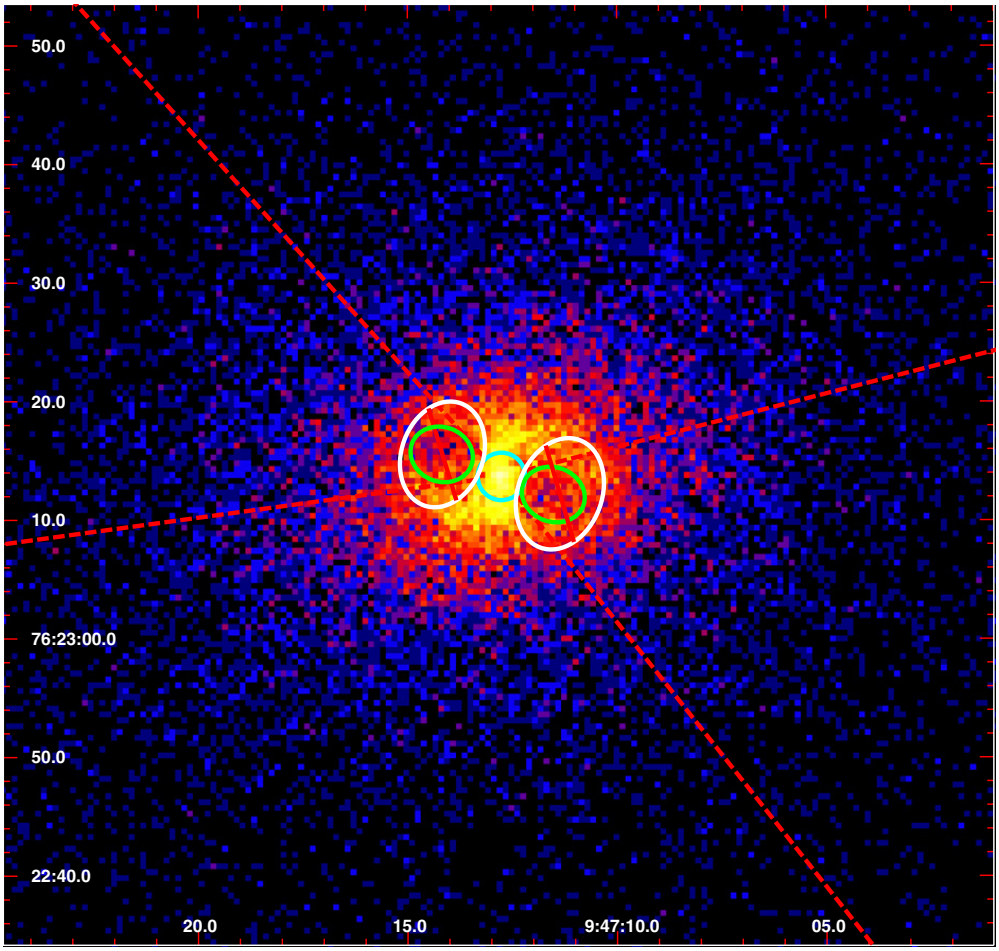

Figure 2. Raw ACIS-S image of RBS 797 in the 0.5–2.0 keV energy interval. The surface brightness profile of the "undisturbed" ICM was obtained by considering 360° annular bins of 1″ width and excluding the white elliptical regions which contain the cavities (green ellipses) and the rims. The red dashed lines delimit the two sectors considered for the surface brightness profile calculated along the cavity directions. See the text for details.

(A color version of this figure is available in the online journal.)

density of the unresolved core is $\simeq 12.9 \pm 0.1$ mJy. The slight difference between the two estimates may be due to the contribution of the short baselines in the combined image with respect to the image in A-array only. To be conservative, we decided to adopt the mean of the two flux densities measured above. We thus estimate that the discrete radio source located at the cluster center has a 1.4 GHz flux density of $\simeq 12.5 \pm 0.5$ mJy, where the errors include the minimum and maximum variation of such an estimate based on our analysis. By subtracting this from the total flux density of the 1.4 GHz emission, we measure a diffuse radio emission of $\simeq 11.5 \pm 0.6$ mJy. The more drastic approach of subtracting the total flux density measured in A-array (17.9 ± 0.2 mJy; Gitti et al. 2006), i.e., the entire radio source filling the X-ray cavities, would still leave a residual $\simeq 6.1 \pm 0.4$ mJy of diffuse radio emission. The variety of methods discussed here demonstrates the difficulty of disentangling the relative contribution of the diffuse emission and of the discrete sources in the total observed radio emission. The nature of the large-scale radio emission, and its possible origin, will be discussed in Section 6.4.

4. *CHANDRA* SPECTRAL ANALYSIS

In each region of interest, a single spectrum was extracted with the CIAO task `specextract` and then grouped to give at least 25 counts in each bin. Only counts deriving from energy bands between 0.5 and 7.0 keV were included. Spectra have been extracted separately from ACIS-S3 and ACIS-I3 observations with independent response matrices and then fitted jointly with the tool `XSPEC` version `12.5.1n`, using a `wabs*apec` model, approximating a collisionally ionized diffuse gas subject to absorption. The hydrogen column density was fixed at the Galactic value ($N_{\rm H} = 2.28 \times 10^{20}$ cm^{-2}; Kalberla et al. 2005) and the redshift was frozen at $z = 0.35$. The metallicity parameter was always allowed to be free and was measured relative to the abundances of Anders & Grevesse (1989). The central circle with radius of 1″.5 (7.2 kpc) contains the central X-ray AGN. In order to avoid contamination with the thermal emission of the ICM, this region was not considered in the spectral fitting. In addition, regions of the cluster lying close to the outer edges of the I3 CCD were excluded, restricting the analysis to the first 125″ (600 kpc). The global cluster temperature, measured in the annulus 1″.5–125″, is $kT = 6.73^{+0.26}_{-0.20}$ keV.

4.1. *Azimuthally Averaged Profiles: Temperature and Metallicity*

A projected radial profile was computed using 10 concentric annuli centered on the cluster core. The radii were selected in order to obtain sufficient counts to constrain the temperature to at least ∼20% accuracy in each annulus (except the outermost

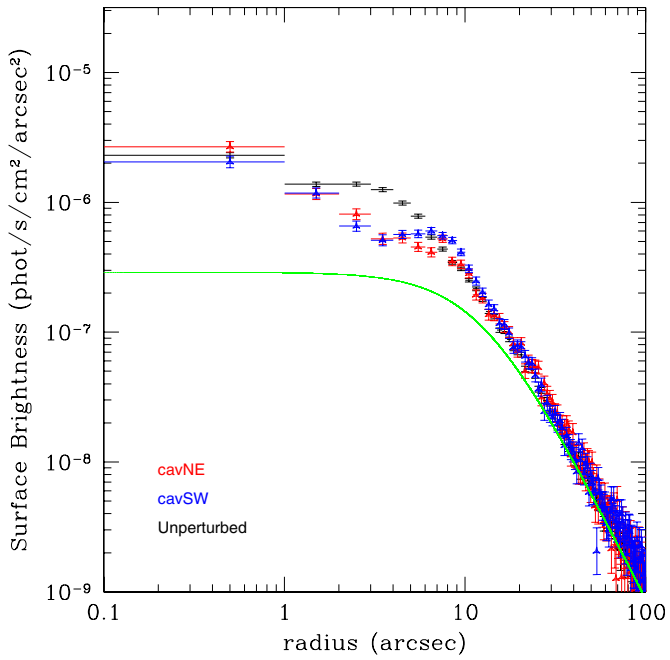

Figure 3. Background subtracted, azimuthally averaged 0.5–2.0 keV radial surface brightness profile of the undisturbed cluster (black crosses), compared with the surface brightness profile along the NE (red triangles) and SW (blue triangles) cavity regions (see Figure 2). Error bars indicate uncertainties at 1σ confidence. Overlaid in green is the fit with a single β-model ($\chi^2_{\rm red} = 0.89$) of the surface brightness profile of the undisturbed cluster. It has been performed in the 25″–110″ radial range and extrapolated to the center.

(A color version of this figure is available in the online journal.)

Table 1
Azimuthally Averaged Spectral Properties

$r1-r2$	r		Source	kT	Z	χ^2/dof
(″)	(″)	(kpc)	(counts)	(keV)	($Z_\odot$)	
1.5–4	2.75	13.2	3856	$4.48^{+0.44(0.26)}_{-0.36(0.24)}$	$0.55^{+0.20(0.12)}_{-0.19(0.11)}$	107.2/115
4–6	5	24	4118	$4.83^{+0.41(0.25)}_{-0.39(0.24)}$	$0.55^{+0.21(0.12)}_{-0.19(0.12)}$	119.2/120
6–8	7	33.6	4120	$5.21^{+0.49(0.27)}_{-0.41(0.25)}$	$0.51^{+0.21(0.13)}_{-0.19(0.12)}$	129.2/123
8–10	9	43.2	3512	$6.12^{+0.68(0.41)}_{-0.66(0.40)}$	$0.44^{+0.21(0.13)}_{-0.20(0.12)}$	130.0/108
10–12	11	52.8	2867	$6.06^{+0.74(0.44)}_{-0.69(0.44)}$	$0.57^{+0.27(0.16)}_{-0.24(0.15)}$	84.4/86
12–16	14	67.2	4619	$7.89^{+1.09(0.58)}_{-0.93(0.57)}$	$0.37^{+0.20(0.12)}_{-0.19(0.12)}$	144.2/137
16–20	18	86.4	3591	$7.92^{+1.16(0.63)}_{-1.01(0.61)}$	$0.45^{+0.24(0.14)}_{-0.23(0.14)}$	99.1/111
20–30	25	120	6099	$7.27^{+0.84(0.50)}_{-0.69(0.47)}$	$0.14^{+0.13(0.08)}_{-0.13(0.08)}$	141.5/172
30–60	45	216	7607	$9.28^{+1.17(0.68)}_{-1.00(0.69)}$	$0.31^{+0.17(0.10)}_{-0.17(0.10)}$	221.0/210
60–125	92.5	444	4897	$11.39^{+3.66(1.90)}_{-2.04(1.35)}$	$0.74^{+0.41(0.24)}_{-0.39(0.23)}$	227.9/215

Notes. Results of the spectral fitting of the 360° annular regions in the 0.5–7.0 keV energy range obtained using the `wabs*apec` model with the absorbing column density fixed to 2.28×10^{20} cm^{-2}. Temperature (in keV), abundances (in fraction of solar value), and normalizations are left as free parameters. The central 1″.5 including the X-ray AGN are excluded from the analysis. The first column lists the delimiting radii for each annulus, while the second and the third list the central value for each bin. Errors are at 90% of confidence level, while those enclosed in brackets are at 1σ.

annulus, see Table 1 for details). The only parameters free to vary in this `wabs*apec` model are the metallicity Z, and the temperature kT. Spectra were fitted in the range 0.5–7.0 keV. The best-fitting parameters and relative errors are listed in Table 1. The measured temperature and metallicity profiles are shown in Figure 5 (upper panels). The temperature values in the outer two annuli are surprisingly high and do not show the decline in the outskirt of the cluster. To test the reliability of these measurements, we adopted as a different background spectrum that extracted in a circular annulus in the outer regions of the two CCDs, finding similar results.

There is an indication of a discontinuity in the projected temperature profile (upper left panel of Figure 5) between the bins 10″–12″ and 12″–16″, which correspond to the region of the rims just outside the cavities. The limited statistics and the edge of the ACIS-I chip do not allow us to measure the behavior of the temperature profile beyond 125″. Therefore, we are not able to observe the decline of the temperature typically observed at larger radii in relaxed clusters (Vikhlinin et al. 2005).

The metallicity profile of RBS 797 (central panel of Figure 2) shows a hint of gradient, with an average abundance of ∼0.4 $Z_\odot$. A more detailed analysis of the azimuthally averaged metallicity profile is not possible due to the large uncertainties.

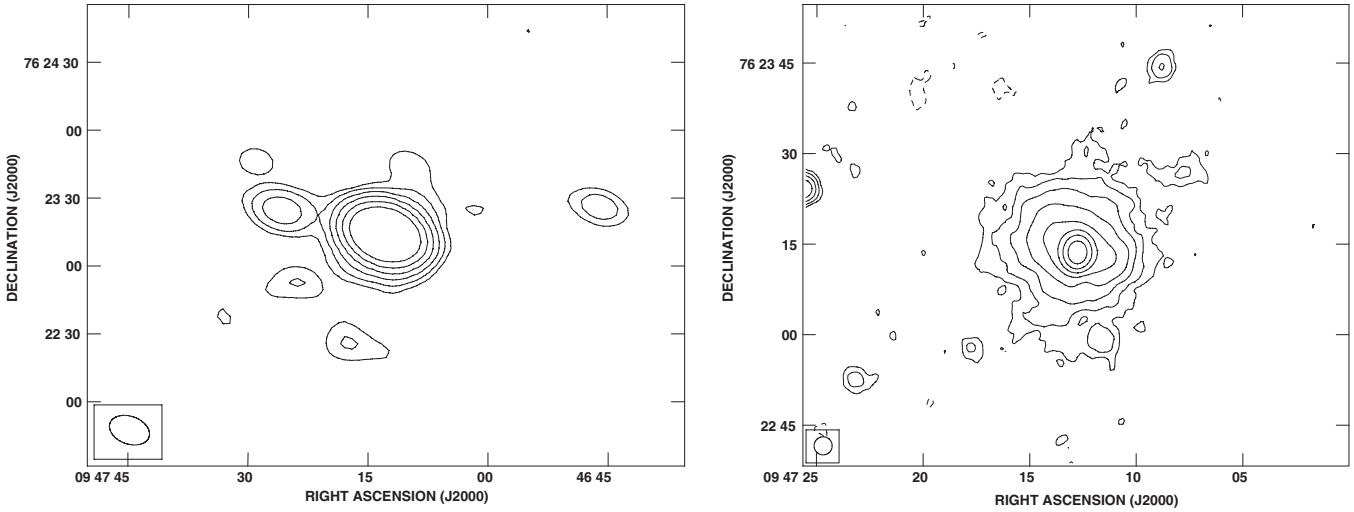

Figure 4. Left: 1.4 GHz VLA (C-array) map of RBS 797 at a resolution of 18″.3 × 12″.2 (the beam is shown in the lower-left corner). The rms noise is 0.03 mJy beam^{-1}. The first contour corresponds to 3σ, the ratio between two consecutive contours being 2. Right: total 1.4 GHz VLA map of RBS 797 at a resolution of 3″ (the beam is shown in the lower-left corner) obtained by combining the observations in A-, B-, and C-array. The rms noise is 0.01 mJy beam^{-1}. The contour levels are −0.035 (dashed), 0.035, 0.070, 0.140, 0.280, 0.560, 1.120, 2.240, 4.480 mJy beam^{-1}.

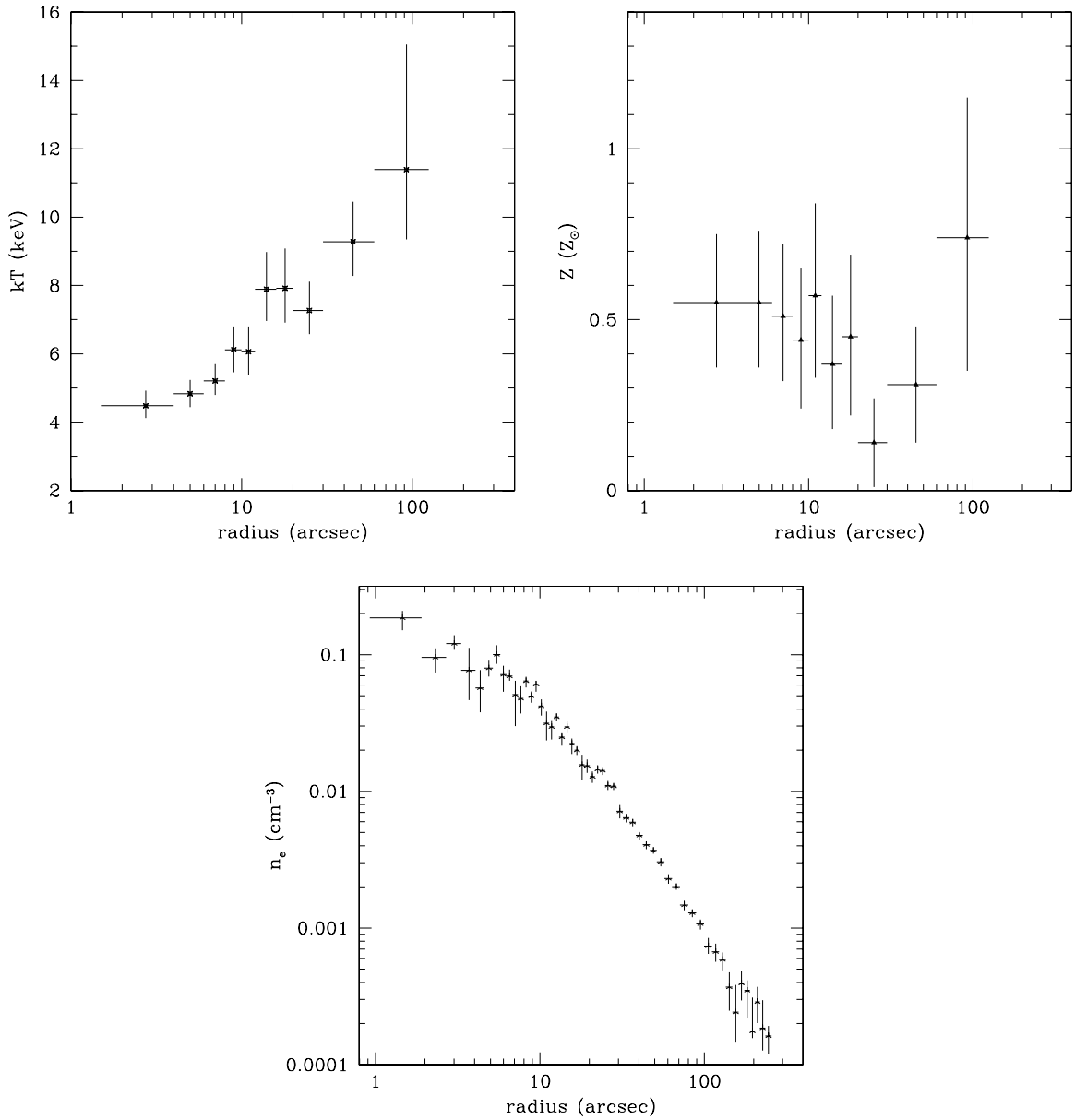

Figure 5. Upper left panel: azimuthally averaged, projected temperature profile obtained by fitting a `wabs*apec` model. The error bars on the *x*-axis indicate the radius of the annulus considered for each bin. Neither the central AGN nor the very external regions of the cluster are considered. Upper right panel: same as the left panel, for the metallicity profile. Lower panel: ICM density profile obtained from the 0.5–2.0 keV surface brightness profile (see the text for details). Vertical bars indicate 1σ errors.

4.2. Deprojection Analysis

Because of the projection effects, the spectral properties at any point in the cluster are the emission-weighted superposition of radiation originating at all points along the line of sight through the cluster. To correct for this effect, we performed a deprojection analysis by adopting the `XSPEC projct` model. We thus fit the spectra extracted in the same ten 360° concentric annular regions adopted for the projected temperature profile (see Section 4.1) with a `projct*wabs*apec` model. Temperature, abundance, and normalization values are free to vary, while the density column and the redshift are frozen at the same values adopted for the `wabs*apec` model.

Results of the deprojection analysis are listed in Table 2. We note that the deprojection analysis increases the error bars without producing significant changes in the global profile shapes. In particular, the metallicity measurement is strongly limited by poor statistics. Therefore, in the following discussion we adopt the projected values of metallicity.

We also derived the density profile by deprojecting the surface brightness profile (see Ettori et al. 2002 for details of the method), obtaining a typical profile of a cool core cluster (Figure 5, lower panel). This is in agreement with the density profile derived from the spectral deprojection analysis (Table 2).

5. COOL CORE ANALYSIS

The X-ray temperature and surface brightness profiles show the evidence of the presence of a cool core in RBS 797. We estimated the cooling time as the time necessary for the ICM to radiate its enthalpy per unit of volume:

$$t_{\rm cool} \approx \frac{H}{n_e n_{\rm H} \Lambda(T)} = \frac{\gamma}{\gamma - 1} \frac{kT}{\mu X_{\rm H} n_e \Lambda(T)}, \qquad (1)$$

Table 2
Deprojected Spectral Analysis

$r1-r2$	r		kT	Z	Norm	n_e
($''$)	($''$)	(kpc)	(keV)	($Z_\odot$)	($\times 10^{-4}$)	($\times 10^{-3}$ cm^{-3})
1.5–4	2.75	13.2	$3.77^{+1.61(0.43)}_{-0.74(0.49)}$	$0.70^{+0.90(0.48)}_{-0.70(0.45)}$	$3.32^{+0.74(0.46)}_{-0.76(0.45)}$	$105.38^{+11.74(7.30)}_{-12.06(7.14)}$
4–6	5	24	$4.61^{+2.19(1.08)}_{-1.06(0.72)}$	$0.51^{+0.98(0.56)}_{-0.51(0.43)}$	$5.46^{+0.90(0.56)}_{-1.21(0.73)}$	$85.35^{+7.03(4.38)}_{-9.46(5.71)}$
6–8	7	33.6	$4.32^{+1.32(0.72)}_{-0.64(0.37)}$	$0.73^{+0.72(0.40)}_{-0.62(0.39)}$	$6.74^{+1.21(0.74)}_{-1.16(0.68)}$	$67.95^{+6.10(3.73)}_{-5.85(3.43)}$
8–10	9	43.2	$6.27^{+2.70(1.53)}_{-1.49(0.97)}$	$0.18^{+0.59(0.34)}_{-0.18(0.18)}$	$6.96^{+0.84(0.55)}_{-0.94(0.37)}$	$53.78^{+3.24(2.12)}_{-3.63(1.43)}$
10–12	11	52.8	$4.44^{+1.21(0.68)}_{-0.73(0.47)}$	$0.88^{+0.59(0.32)}_{-0.58(0.34)}$	$5.63^{+1.02(0.57)}_{-1.03(0.62)}$	$39.60^{+3.59(2.00)}_{-3.62(2.18)}$
12–16	14	67.2	$8.26^{+2.10(1.55)}_{-2.01(1.36)}$	$0.26^{+0.36(0.23)}_{-0.26(0.25)}$	$8.67^{+0.84(0.39)}_{-0.84(0.44)}$	$27.25^{+1.32(0.61)}_{-1.32(0.69)}$
16–20	18	86.4	$7.54^{+1.84(1.16)}_{-1.34(0.91)}$	$0.83^{+0.46(0.30)}_{-0.48(0.32)}$	$7.31^{+0.81(0.48)}_{-0.83(0.50)}$	$19.49^{+1.08(0.64)}_{-1.11(0.67)}$
20–30	25	120	$7.21^{+1.12(0.68)}_{-0.82(0.53)}$	$0.08^{+0.17(0.10)}_{-0.08(0.08)}$	$15.90^{+0.66(0.43)}_{-0.72(0.38)}$	$13.03^{+0.27(0.18)}_{-0.29(0.16)}$
30–60	45	216	$9.03^{+1.41(0.85)}_{-1.08(0.71)}$	$0.26^{+0.19(0.10)}_{-0.19(0.12)}$	$16.76^{+0.73(0.44)}_{-0.72(0.43)}$	$4.24^{+0.09(0.06)}_{-0.09(0.05)}$
60–125	92.5	444	$12.33^{+3.85(2.36)}_{-2.40(1.74)}$	$0.74^{+0.36(0.20)}_{-0.39(1.17)}$	$11.77^{+1.04(0.61)}_{-0.88(0.55)}$	$1.17^{+0.05(0.03)}_{-0.04(0.03)}$

Notes. Results of the deprojected analysis of the 360° annular regions in the 0.5–7.0 keV energy range previously used for the study of the projected temperature profile. These data are obtained using the `projct*wabs*apec` model, fixing the absorbing column density to 2.28×10^{20} cm^{-2}. Temperature (in keV), abundances (in fraction of solar value), and normalizations are left as free parameters. The first central 1.″5 are excluded from the analysis. The result of the fit gives $\chi^2/\mathrm{dof} = 1418.40/1400$. Densities have been derived from the `apec` normalization: $10^{-14} n_e n_{\rm H} V/4\pi [D_A(1+z)]^2$, assuming $n_p = 0.82 n_e$. Errors are at 90% of confidence level, while those enclosed in brackets are at 1σ.

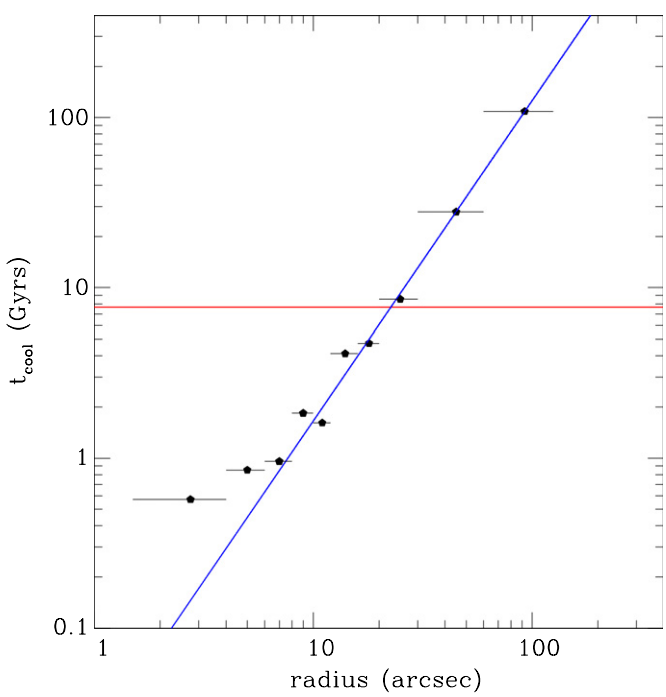

Figure 6. Cooling time profile measured from the spectral deprojected analysis. The red line indicates the value of 7.7×10^9 yr which is assumed to be the cluster age. The blue line is the power-law fit to the cooling time radial profile. The corresponding value of the cooling radius is $r_{\rm cool} \simeq 22.''7$ ($\simeq$109 kpc).

(A color version of this figure is available in the online journal.)

where $\mu \approx 0.61$ is the molecular weight for a fully ionized plasma, $\gamma = 5/3$ is the adiabatic index, $X_{\rm H} \approx 0.71$ is the hydrogen mass fraction, and $\Lambda(T)$ is the cooling function. By adopting the values of the temperature and electron density derived from the spectral deprojection analysis (see Section 4.2), we derive the radial profile of the cooling time (Figure 6), which shows a power-law behavior. The fit with a power law gives $t_{\rm cool} \propto r^{1.88}$. The central cooling time, estimated in the first bin (1.″5–4″), is $t_{\rm cool} = 5.7 \times 10^8$ yr.

It is also possible to estimate the cooling radius, defined as the radius within which the gas has a cooling time less than the age of the system. The choice of the method adopted to estimate such an age is arbitrary. For consistency with the assumption usually made for local clusters, we adopt the cluster's age to be 7.7×10^9 yr (the look-back time at the epoch $z = 1$, at which many clusters appear to be relaxed and a CF could establish itself). We thus estimate $r_{\rm cool} \simeq 22.''7$ (Figure 6), corresponding to $\simeq$109 kpc. Our estimate of $r_{\rm cool}$ is slightly different from that of Rafferty et al. (2006) and Cavagnolo et al. (2011) due to the different definition of $t_{\rm cool}$ used.

The spectrum extracted within the cooling radius (excluding the central 1.″5) was fitted with `XSPEC` using a deprojected multi-phase model (`projct*wabs*(apec+mkcflow)`). The only difference from the model adopted in the deprojection analysis in Section 4.2 is the addition of an isobaric multi-phase component (`mkcflow`). The `apec` parameters of temperature and abundance were left free to vary, as well as the absorbing column density which was tied between all the annuli. For the `mkcflow` model, the high temperature (high T) and abundance were tied to the corresponding values for the `apec` model, for which the parameters are free. On the other hand, the low temperature (low T) was fixed at ~0.1 keV as we are assuming the physics of a standard CF model.

The best-fit parameters give a mass deposition rate of the CF, calculated from the `mkcflow` normalization, of $\dot{M} = 231^{+316}_{-227}\ M_\odot$ yr^{-1} (consistent with Rafferty et al. 2006), a deprojected CF temperature of $kT_{1.''5-22.''7} = 5.77^{+0.42}_{-0.38}$ keV and a cooling X-ray luminosity inside the cooling radius within the energy range 0.5–7 keV of $L_{X,\rm cool} = 1.33 \times 10^{45}$ erg s^{-1}. The high nominal value of the mass deposition rate that we estimate in the framework of the standard CF model is likely due to the temperature gradient seen in the profile (upper left panel of Figure 5), since the temperature within the cooling radius is clearly lower than the values found at outer radii. Nevertheless, for comparison with the literature which adopted the standard CF model, we use this value of the mass deposition rate for estimating the CF power presented in Section 6.4.

6. DISCUSSION

6.1. Energetics

The comparison between the X-ray luminosity of the ICM within the cooling radius and the cavity power provides us with an estimate of the balance between the energy losses of the ICM by the X-ray emission and the cavity heating (Bîrzan et al. 2004; Rafferty et al. 2006). The bolometric X-ray luminosity inside the cooling region is estimated from a spectral deprojection analysis as $L_{X,\mathrm{cool}} = 1.33 \times 10^{45}$ erg s^{-1}, consistent with the estimate of Rafferty et al. (2006).

The power of the cavities P_{cav} is given by the ratio of the cavity energy and the cavity age. The energy required to create a cavity with pressure p and volume V is the sum of the pV work done by the jet to displace the X-ray emitting gas while it inflates the radio lobes, and the internal energy E of the cavity system. This quantity is the enthalpy defined as

$$E_{\mathrm{cav}} = H = E + pV = \frac{\gamma}{\gamma - 1} pV, \quad (2)$$

where $\gamma = 4/3$ for relativistic plasma. Pressure and volume can be estimated directly by X-ray observations through measurements of the cavity size and of the temperature and density of the surrounding ICM. A potential issue is the uncertainty in determinations of the cavity volumes. The cavity size is usually estimated through a visual inspection of the X-ray images. This method is therefore dependent on the quality of the X-ray data and is also prone to systematic error. Furthermore, projection affects the determination of the actual spatial geometry of the cavity system. The cavity size and geometry measured by different observers may vary significantly depending on the approach adopted, leading to differences between estimates of up to a factor of a few in pV (e.g., Gitti et al. 2010; O'Sullivan et al. 2011; Cavagnolo et al. 2011). Here, we estimate the cavity size from the surface brightness profile of the central region of the cluster. From the decrement of the surface brightness observed within the two X-ray deficient regions containing the lobes (Figure 3), we estimated the extent of the major axis of the two ellipses. The surface brightness in the directions of the cavities clearly falls below that of the undisturbed cluster within the ∼2″–7″ radius.

For the estimate of the ICM pressure ($p \simeq 1.92 n_e kT$) surrounding the cavities, we considered the electron density and temperature within the bin 4″–6″ in the cluster profiles (upper and lower panels of Figure 5). We calculated that the total enthalpy of the cavity system is $E_{\mathrm{cav}} = 1.68 \times 10^{60}$ erg. For the estimate of the cavity age, we adopted the sound crossing time, defined as $t_{\mathrm{sound}} \approx R/c_s$, where R is the distance of the center of the cavity from the central radio source and c_s is the sound speed. Finally, we find the total cavity power of $P_{\mathrm{cav}} = 2.49 \times 10^{45}$ erg s^{-1}. The cavity properties are listed in Table 3.

Although we estimate slightly smaller cavity volumes and we adopt a different assumption for the cavity age (sound crossing time instead of buoyancy time), we find values of energy and power of the cavities consistent with those of the *configuration-I* in Cavagnolo et al. (2011).

Table 3
Cavity Properties

	Cavity NE	Cavity SW
a (″)	2.67	2.70
b (″)	2.30	2.29
R (″)	5.37	4.62
a (kpc)	12.82	12.96
b (kpc)	11.04	10.99
R (kpc)	25.78	22.18
V (cm^3)	1.93×10^{68}	1.93×10^{68}
p (erg cm^{-3})	1.09×10^{-9}	1.09×10^{-9}
kT (keV)	4.61	4.61
pV (erg)	2.10×10^{59}	2.10×10^{59}
E_{cav} (erg)	8.41×10^{59}	8.41×10^{59}
t_{sound} (yr)	2.31×10^{7}	2.02×10^{7}
P_{cav} (erg s^{-1})	1.15×10^{45}	1.34×10^{45}

Notes. Results of the analysis of the cavity system of RBS 797. We assume the shape of the cavities as prolate ellipsoids. The cavity energy is measured as $E_{\mathrm{cav}} = 4pV$ and the cavity power is estimated as $P_{\mathrm{cav}} = E_{\mathrm{cav}}/t_{\mathrm{sound}}$.

6.2. Evidence for Metal-enriched Outflows

Hydrodynamic simulations (e.g., Brüggen 2002; Roediger et al. 2007; Mathews & Brighenti 2008) predicted that in cool core clusters with a cavity system, the ICM in the core is stirred. Jets from the central source in clusters of galaxies can contribute both to quench the deposition of cold gas and to induce motions affecting the metallicity profile. Moreover, Gaspari et al. (2011a, 2011b) show new detailed models of AGN-injected jets which uplift the metal-enriched gas in the core by feedback cycles. These are split in two phases during the outburst; initially, the gas with higher abundance lies asymmetrically along the jet axis, followed by a phase of turbulence and mixing. Gaspari et al. (2011a, 2011b) estimate that the maximum distance along the cavity axis at which the enriched gas could be spread is ∼40 kpc, and that the contrast of the iron abundance in the cavity directions with that in the rest of the ICM is ∼0.1–0.2.

In RBS 797, we find differences in the iron abundance distribution, depending on direction. We considered four sectors delimited by a variable outer radius starting from the same 1.″5 inner radius (see Figure 7). In our analysis, we consider the N and the S sectors as unperturbed, since they enclose only the regions of the cluster in which the ICM distribution does not show special features such as the cavities. The first analysis is performed in the annulus from 1.″5 to 12″, while the second outer radius was set at 15″ and the last at 30″. As for the study of the azimuthally averaged temperature profile, the temperature, abundance, and normalization were left free to vary, while redshift and gas column density were fixed to the same values previously used in Section 4.1. Spectra were fitted with a single plasma model for a collisionally ionized diffuse gas.

The results in Table 4 and Figure 8 indicate higher metallicity along the NE and SW cavity directions compared to the unperturbed N sector in all the three annuli (at 1σ error). In the biggest annulus (1.″5–30″), the NE sector shows higher abundance compared to both the unperturbed N and S regions. Combining spectra from the two cavity sectors in a joint fit and comparing to the results of fitting the two unperturbed sectors supports the relationship between metallicity and direction (see the lower section of Table 4 for details).

Likely, the AGN outburst may have lifted the cooler, metal-rich gas from the central region to larger radii along the directions of the inflating cavities. We found that, taking into account three different outer radii, the cavity sectors have higher abundances than the unperturbed regions, at 1σ confidence. So, this behavior also persists at larger radii and not only nearby the cavity system. This effect has been found in other systems

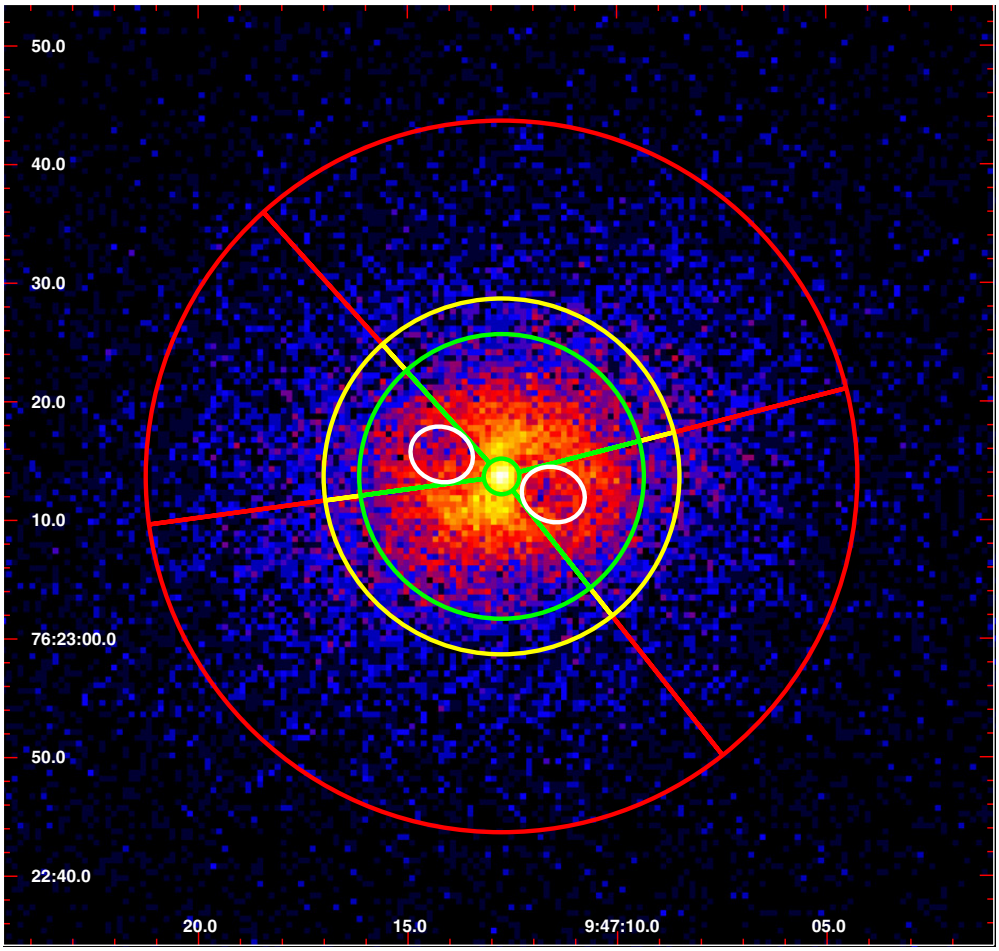

Figure 7. Raw image of RBS 797 in the 0.5–7.0 keV energy range showing the subdivision in the four wedges used in the study of the iron abundance variations. The white ellipses indicate the cavities. The four sectors are tangent to the cavities and divide the cluster in two unperturbed regions (N and S) and two cavity regions (NE and SW). The angular apertures of each region are NE $\sim 56^\circ$, SW $\sim 66^\circ$, N $\sim 118^\circ$, and S $\sim 120^\circ$. The measurements of the metallicity were taken in three annuli which differ only for the length of the external radius (see Table 4). The green sectors indicate the $1''.5$–$12''$ selection while the yellow indicate the $1''.5$–$15''$ bin, and the more external red lines represent the biggest radius at $1''.5$–$30''$.

(A color version of this figure is available in the online journal.)

(e.g., M87, Simionescu et al. 2008; Hydra A, Kirkpatrick et al. 2009, Simionescu et al. 2009b; NGC 5813, Randall et al. 2011). In particular, recent work by Kirkpatrick et al. 2011 shows a correlation between jets and metallicity.

6.3. Evidence for Hot Cavities

In Section 6.2, we described the analysis of the azimuthal variations of the ICM properties. Here, we want to perform a more detailed analysis of the projected temperature in the cavities and in the surrounding gas. We extracted the spectra separately in both the cavities, and in each sector surrounding a single cavity (clearly excluding the cavities). Spectra were then fitted with the model `wabs*apec` in `XSPEC`, with the temperature and abundance as free parameters and column density set at the Galactic value. Considering the regions of Figure 9, in the cavities we found projected temperatures (1σ errors) of $kT_{\rm cavNE} = 5.86^{+0.91}_{-0.79}$ keV for the NE cavity and $kT_{\rm cavSW} = 5.71^{+0.92}_{-0.72}$ keV for the SW cavity. These have been compared with the $kT_{\rm gasNE} = 4.62^{+0.24}_{-0.23}$ keV and $kT_{\rm gasSW} = 5.08^{+0.25}_{-0.24}$ keV, respectively, the values for the gas surrounding the NE and the SW cavities. Since these results do not provide definite constraints due to the low statistics of the selected regions, we tried to combine together the two cavities and compare them to the combined spectra of the external gas. The results of the joint fits give an indication for hotter cavities: $kT_{\rm gas} = 4.84^{+0.17}_{-0.17}$ keV and in the cavities $kT_{\rm cav} = 5.27^{+0.59}_{-0.40}$ keV.

We performed an additional test by means of a "softness ratio" (SR), which is defined as SR $= (S - H)/(S + H)$, where S and H are the count rates in the soft and in the hard band, respectively. After extracting the surface brightness profile in the cavity system and in the external gas, both in the X-ray soft (0.5–2.0 keV) and hard (2.0–7.0 keV) energy band, we compared their SRs. The SR method can be used as an indicator of the temperature, since higher SR values would imply the prevalence of the soft emission, thus lower projected temperatures. We found that the regions surrounding the cavities have an SR slightly higher than that of the cavities: $\mathrm{SR}_{\rm cav} = 0.5468 \pm 0.0216$, $\mathrm{SR}_{\rm gas} = 0.5747 \pm 0.0093$. This means that the relative quantity of soft photons is higher in the outer gas, indicating that the cavities are hotter than the surrounding ICM.

Finally, we made a further attempt to compare the projected temperature within the cavities with that of the gas in the other directions. We considered four sectors, two along the cavity directions and two in the perpendicular unperturbed regions, excluding the cavity rims from the selection. Based on the unsharp masked image (right panel of Figure 1), we divided

Table 4
Abundance Variations

Sectors	$r1-r2$	r		Source	kT	Z	χ^2/dof
(°)	(″)	(″)	(kpc)	(counts)	(keV)	($Z_\odot$)	
NE (cav) [∼56°]	1.5–12	6.75	32.4	2381	$5.36^{+0.72(0.41)}_{-0.52(0.32)}$	$0.82^{+0.38(0.22)}_{-0.33(0.24)}$	66.3/73
	1.5–15	8.25	39.6	2996	$5.77^{+0.71(0.43)}_{-0.55(0.38)}$	$0.65^{+0.28(0.17)}_{-0.26(0.16)}$	88.1/90
	1.5–30	15.75	75.6	4886	$5.91^{+0.58(0.34)}_{-0.53(0.33)}$	$0.57^{+0.20(0.12)}_{-0.19(0.11)}$	123.1/143
N [∼118°]	1.5–12	6.75	32.4	6154	$4.98^{+0.33(0.21)}_{-0.33(0.20)}$	$0.37^{+0.13(0.08)}_{-0.13(0.08)}$	134.0/164
	1.5–15	8.25	39.6	7307	$5.26^{+0.39(0.11)}_{-0.32(0.19)}$	$0.37^{+0.12(0.07)}_{-0.12(0.07)}$	162.3/180
	1.5–30	15.75	75.6	10622	$5.84^{+0.39(0.10)}_{-0.38(0.10)}$	$0.35^{+0.10(0.06)}_{-0.10(0.06)}$	186.3/221
SW (cav) [∼66°]	1.5–12	6.75	32.4	3363	$5.25^{+0.62(0.34)}_{-0.45(0.27)}$	$0.61^{+0.24(0.14)}_{-0.22(0.14)}$	77.1/102
	1.5–15	8.25	39.6	4121	$5.27^{+0.56(0.31)}_{-0.40(0.24)}$	$0.66^{+0.22(0.13)}_{-0.20(0.13)}$	104.9/122
	1.5–30	15.75	75.6	6319	$5.96^{+0.49(0.28)}_{-0.47(0.29)}$	$0.47^{+0.15(0.09)}_{-0.15(0.09)}$	126.2/171
S [∼120°]	1.5–12	6.75	32.4	6661	$5.21^{+0.40(0.20)}_{-0.32(0.20)}$	$0.50^{+0.15(0.09)}_{-0.14(0.08)}$	199.1/172
	1.5–15	8.25	39.6	7873	$5.31^{+0.42(0.22)}_{-0.30(0.18)}$	$0.48^{+0.13(0.08)}_{-0.12(0.07)}$	219.9/191
	1.5–30	15.75	75.6	11349	$6.04^{+0.37(0.22)}_{-0.36(0.22)}$	$0.38^{+0.10(0.06)}_{-0.10(0.06)}$	253.1/235
NE + SW	1.5–12	6.75	32.4	5743	$5.31^{+0.47(0.26)}_{-0.34(0.21)}$	$0.68^{+0.20(0.12)}_{-0.19(0.12)}$	144.0/177
	1.5–15	8.25	39.6	7286	$5.60^{+0.44(0.27)}_{-0.36(0.24)}$	$0.64^{+0.17(0.10)}_{-0.16(0.10)}$	219.0/223
	1.5–30	15.75	75.6	11487	$6.03^{+0.36(0.22)}_{-0.35(0.22)}$	$0.51^{+0.12(0.07)}_{-0.12(0.07)}$	290.3/331
N + S	1.5–12	6.75	32.4	12812	$5.10^{+0.24(0.14)}_{-0.23(0.14)}$	$0.43^{+0.10(0.06)}_{-0.09(0.06)}$	335.4/338
	1.5–15	8.25	39.6	15628	$5.32^{+0.28(0.14)}_{-0.21(0.13)}$	$0.43^{+0.09(0.05)}_{-0.09(0.05)}$	470.3/392
	1.5–30	15.75	75.6	22541	$6.00^{+0.26(0.16)}_{-0.26(0.16)}$	$0.37^{+0.07(0.04)}_{-0.07(0.04)}$	570.9/483

Notes. Upper section: results of the spectral analysis in the 0.5–7.0 keV energy range of the four sectors tangent to the cavities (Figure 7). Lower section: results obtained by extracting the combined spectra of the two sectors containing the cavities (NE and SW), and the two undisturbed sectors (N and S), respectively. The first column lists the delimiting radii for each annulus, while the second and the third columns list the central value for each bin. Errors are at 90% of confidence level, while those enclosed in brackets are at 1σ.

Table 5
Softness Ratio

	Bin	$\frac{S-H}{S+H}$	
		Cavity NE	Cavity SW
Cavities	(a)	0.1522 ± 0.0420	0.3561 ± 0.0628
	(b)	0.5695 ± 0.0266	0.5349 ± 0.0233
	(c)	0.4915 ± 0.0335	0.5461 ± 0.0232
No-cavities	(a)	0.4028 ± 0.0297	0.2203 ± 0.0444
	(b)	0.5948 ± 0.0141	0.6007 ± 0.0138
	(c)	0.5139 ± 0.0255	0.5242 ± 0.0219

Notes. Values of the softness ratio calculated in each annulus. The considered bins (values (a), (b), (c)) are different for the two cavities and are better visualized in Figure 10.

the NE and the SW sectors in three annuli tangent to the inner and outer edge of the cavities (Figure 10). The first bin goes from the center of the cluster to the beginning of the cavity (0″–2.″7 for the NE and 0″–1.″9 for the SW directions, (a) sectors in Figure 10), the second embodies the whole cavities (2.″7–8.″1 for NE and 1.″9–7.″3 for SW, (b) sectors in Figure 10) and the last includes the rims (8.″1–11″ for NE and 7.″3–11″ for SW, (c) sectors in Figure 10). SRs for these regions are listed in Table 5. In Figure 11, we compare the SR of the unperturbed sectors with the values of the NE cavity sector (left panel) and with the SW cavity region (right panel). Looking at the second bin in both the plots of Figure 11, we find further support for the indication that the gas in the cavities of RBS 797 is hotter than the surrounding ICM, as previously found in other clusters of galaxies such as 2A 0335+096 (Mazzotta et al. 2003), MS 0735+7421 (Gitti et al. 2007a), and M87 (Million et al. 2010).

Despite our detailed study of the cavities and surroundings temperatures, what we found here may only be a projection effect. The hotter gas along our line of sight through the cavities could have a greater impact on the spectra of the cavities than on those of the brighter gas surrounding them (the rims), making the cavities to appear hotter. Furthermore, the cavities are likely to be regions from which the (cooler) X-ray emitting gas has been pushed out, so a larger fraction of the emission along our line of sight may be coming from the projected hotter gas at larger radii. We performed a further test in order to investigate whether the X-ray emission of the cavities along our line of sight is due exclusively to the outer gas emission, or not. From the surface brightness and density profiles (Figure 3 and the lower panel of Figure 5, respectively), we found an average density of ∼0.075 cm^{-3} and a counts estimate of ∼5.4 counts s^{-1} arcmin^{-2} in the annular region containing the cavities. Therefore, at the ambient density and temperature, we expect to have ∼119 counts s^{-1} with ACIS-S3 chip in the 0.5–7.0 keV energy band, with the `apec` normalization ($K_{\rm apec}$) set to unity. Considering a spherical volume approximately equal to the volume of the cavities and solving the equation for the `apec` normalization, we estimated $K_{\rm apec} \simeq 4.78 \times 10^{-5}$. From this spherical volume of unperturbed gas located at the cavity position, we would thus measure an emission of ∼1.04 counts s^{-1} arcmin^{-2} that, with the exposure time of the ACIS-S3 observation ($t_{\rm exp,S3} \simeq 36$ ks), is equivalent

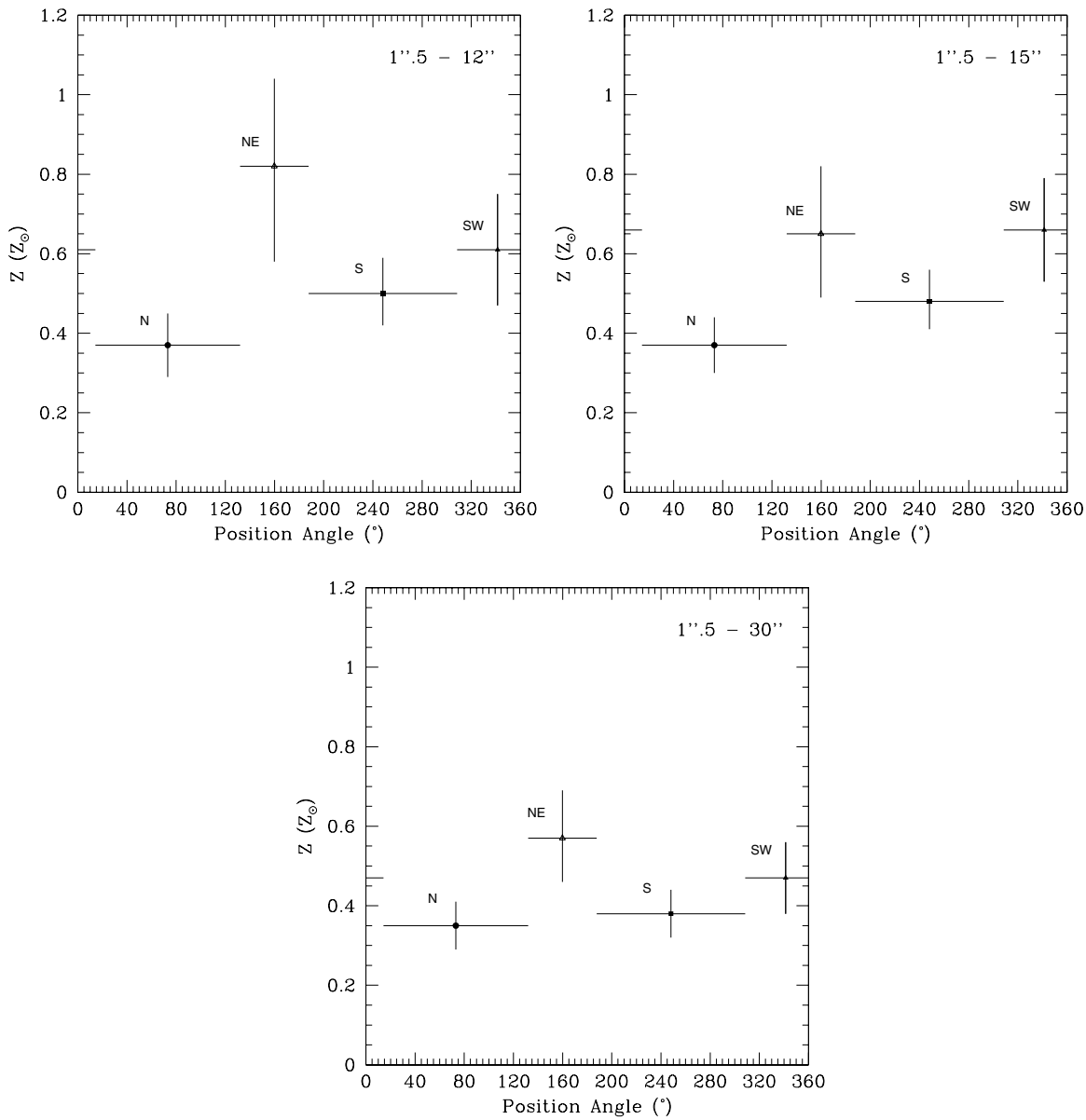

Figure 8. Metallicity values (from Table 4) as a function of the mid-aperture angle of the sector in three different annuli: 1.″5–12″ (upper left panel), 1.″5–15″ (upper right panel), and 1.″5–30″ (lower panel). The 0° angle is defined along the W direction and the aperture angle increases counterclockwise. Here the four wedges are taken singularly: the full triangle indicates the value in the SW cavity, the circle that in the N region, the empty triangle that in the NE cavity and square that in the S region. The regions considered are shown in Figure 7. Error bars are at 1σ.

to ∼206 counts. We considered several regions outside the cavity directions having the same cavity area and located at the same distance from the center, and we estimated the average number of counts from the 0.5–7.0 keV image. We found that the difference between the average number of counts within these regions (∼1140) and the average number of counts inside the cavities (∼766) exceeds the number of counts originating from the estimated contribution of the unperturbed gas inside the cavities. As a zero-order test, this indicates that there is no emission related to the cavities, so that they can be considered devoid of X-ray emitting gas. Unfortunately, the poor statistics did not allow us to test this hypothesis with some more complicated spectral models, such as deprojection analysis.

6.4. Large-scale Radio Emission

The radio properties of RBS 797 presented in Section 3.2 are consistent with a scenario of three distinct outbursts, with the jet axis precessing ∼90° between outbursts, with a period of $\sim 10^7$ yr. The X-ray observations show features that are consistent with this picture: the northeast–southwest inner cavities and the elliptical inner edge revealed by the *Chandra* images (Figure 1) could be associated with the intermediate outburst; the outer edge shown by *Chandra* (Figure 1) could be associated with the oldest outburst. Alternatively, the observed change in the orientation of the radio axis, most evident between the inner 4.8 GHz jets and the 1.4 GHz emission filling the cavities (black and green contours in Figure 12, right panel, see also Figure 4 of Gitti et al. 2006), may be due to jet deflection. Jet deflection is caused either by ICM pressure gradients or by dense regions of cold gas that may have been ionized by massive stars born in a starburst triggered by the CF (e.g., Salomé & Combes 2003). The existing data do not allow us to discriminate between these two possibilities.

On the other hand, the fact that the total size of the large-scale radio emission is comparable to that of the cooling region

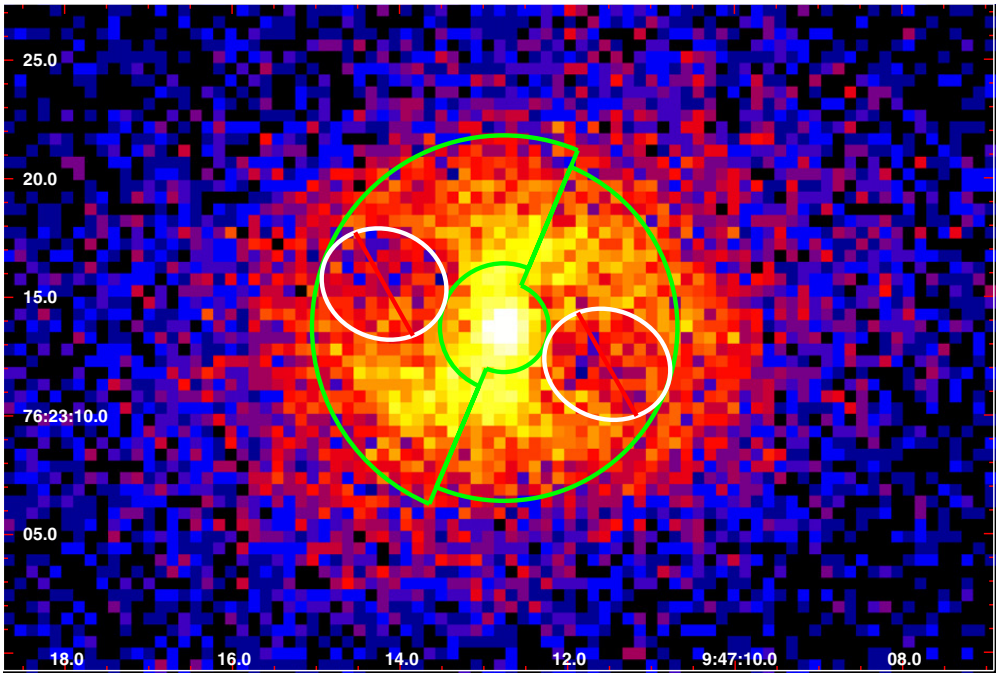

Figure 9. Regions considered to estimate the projected temperature in the gas (green) surrounding the cavity system, overlaid on the 0.5–7.0 keV raw image of the core of RBS 797. The dimensions of the cavities (white) are listed in Table 3.

(A color version of this figure is available in the online journal.)

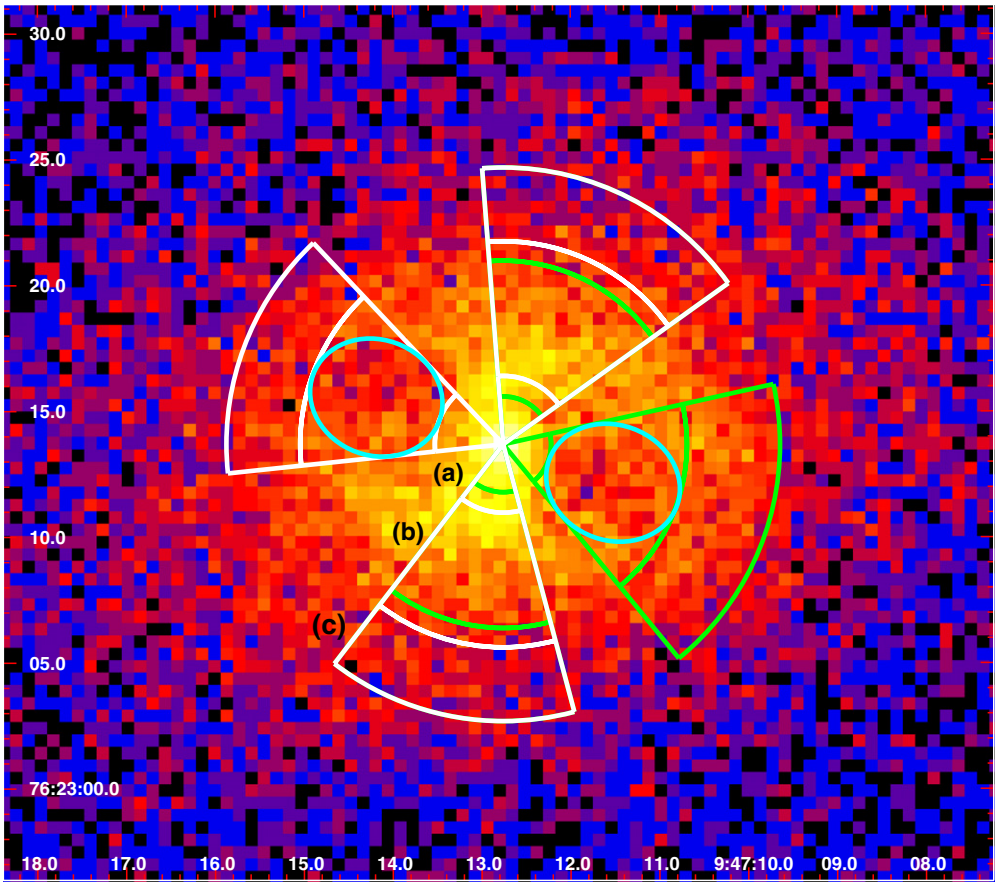

Figure 10. Regions adopted to estimate the softness ratio. Three bins are selected in order to calculate the softness ratio in three regions: (a) from the center of the cluster to the inner edge of the selected cavity (cyan ellipses); (b) encloses the whole cavity; and (c) from the outer edge of the cavity to the end of the rims. The radii of the three bins are different for the two cavities, while the aperture angles are the same in both cases. The bins for the NE cavity (white regions) are (a) 0″–2.″7; (b) 2.″7–8.″1; and (c) 8.″1–11″. The bins used for the SW cavity (green regions) are (a) 0″–1.″9; (b) 1.″9–7.″3; and (c) 7.″3–11″.

(A color version of this figure is available in the online journal.)

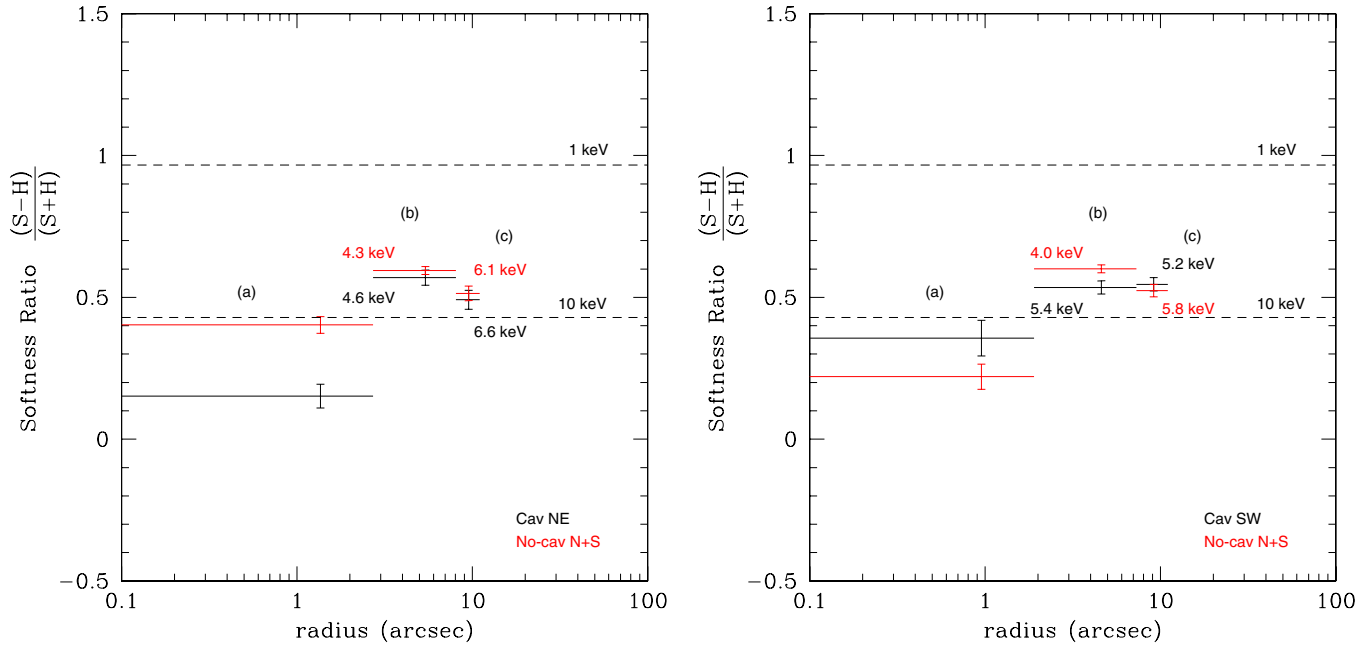

Figure 11. Softness ratio as an indicator of the temperature. We have considered three bins, different in each cavity direction. The wedges corresponding to the (a), (b), and (c) bins are shown in Figure 10. The dimensions of the annuli of the unperturbed regions are taken equal to those of the region with which are compared, while their angular aperture does not vary. The dashed lines give useful hints about the corresponding temperatures. Uncertainties are taken at 1σ confidence.

(A color version of this figure is available in the online journal.)

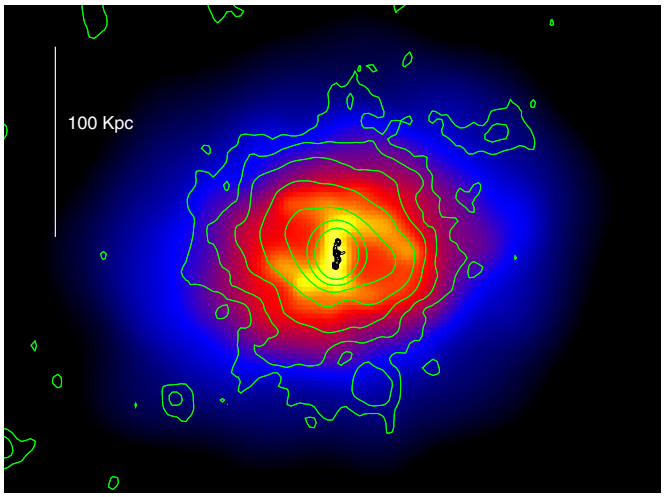

Figure 12. 1.4 GHz VLA radio contours at a resolution of 3″ (green, see Figure 4, right panel) and 4.8 GHz VLA radio contours at a resolution of 0.″4 (black, see Figure 2 of Gitti et al. 2006) overlaid onto the smoothed *Chandra* X-ray image of RBS 797. Smoothing of the *Chandra* ACIS-S3 was obtained adaptively in the 0.5–7.0 keV energy range. It was obtained by the task `csmooth` setting the signal-to-noise ratio (S/N) at value 3.

(A color version of this figure is available in the online journal.)

suggests a different interpretation, which would be consistent with either jet precession or jet deflection: that RBS 797 hosts a diffuse radio mini-halo. Mini-halos are diffuse radio sources, extended on a smaller scale (up to ∼500 kpc), surrounding a dominant radio galaxy at the cluster center. They are generally only observed in cool core clusters and it has been found that these sources are not connected to ongoing cluster major merger activity. Their radio emission is indicative of the presence of diffuse relativistic particles and magnetic fields in the ICM, since these sources do not appear as extended lobes maintained by an AGN, as in classical radio galaxies (Giovannini & Feretti 2002). In particular, due to the fact that the radiative lifetime of radio-emitting electrons ($\sim 10^8$ yr) is much shorter than any reasonable transport time over the cluster scale, the relativistic electrons responsible for the extended radio emission from mini-halos need to be continuously re-energized by various mechanisms associated with turbulence in the ICM (reaccelerated *primary* electrons), or freshly injected on a cluster-wide scale (e.g., as a result of the decay of charged pions produced in hadronic collisions, *secondary* electrons).

Gitti et al. (2002) developed a theoretical model which accounts for the origin of radio mini-halos as related to electron reacceleration by MHD turbulence in CFs. In this model, the necessary energetics to power radio mini-halos is supplied by CFs themselves, through the compressional work done on the ICM and the frozen-in magnetic field. This supports a direct connection between CFs and radio mini-halos. Although secondary electron models have been proposed to explain the presence of their persistent, diffuse radio emission on large scale in the ICM (e.g., Pfrommer & Enßlin 2004; Keshet & Loeb 2010), the observed trend between the radio power of mini-halos and the maximum power of CFs (Figure 13) has given support to a primary origin of the relativistic electrons radiating in radio mini-halos, favored also by the successful, detailed application of the model of Gitti et al. (2002) to two cool core clusters (Perseus and A 2626; Gitti et al. 2004) and by recent statistical studies (Cassano et al. 2008). However, the origin of the turbulence necessary to trigger the electron reacceleration is still debated. The signatures of minor dynamical activity have recently been detected in some mini-halo clusters, thus suggesting that additional or alternative turbulent energy for the reacceleration may be provided by minor mergers (Gitti et al. 2007b; Cassano et al. 2008) and related gas sloshing mechanism in cool core clusters (Mazzotta & Giacintucci 2008; ZuHone et al. 2011). Given the prevalence of mini-halos in clusters with X-ray cavities, another attractive possibility is that the turbulent energy is provided by a small fraction of the energy released by

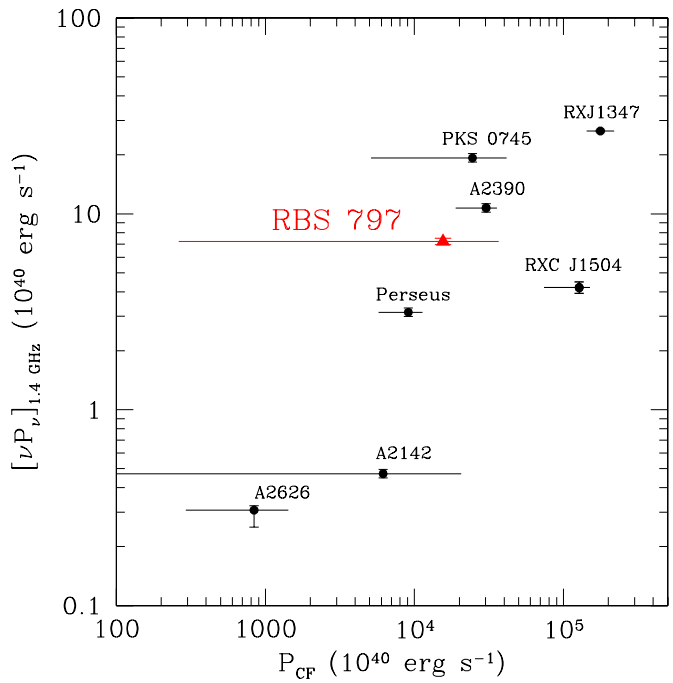

Figure 13. Cooling flow power, calculated as $P_{\rm CF} = \dot{M}kT/\mu m_p$ vs. the integrated radio power νP_ν at 1.4 GHz. The other objects plotted with RBS 797 (red triangle) are galaxy clusters whose diffuse radio emission size is comparable to the cooling radius, all taken from the literature (Gitti & Schindler 2004; Gitti et al. 2007a; Böhringer et al. 2005; Giacintucci et al. 2011). When necessary, the values have been rescaled to the cosmology adopted in this paper.

(A color version of this figure is available in the online journal.)

the lobes rising from the central AGN (as suggested by Cassano et al. 2008).

We can test qualitatively the consistency of the observational X-ray and radio properties of RBS 797, with the trend between the radio power on the mini-halos and the maximum power of the CFs expected by the reacceleration model. This has been observed in a first sample of mini-halos selected by Gitti et al. (2004), who found that the strongest radio mini-halos are associated with the most powerful CFs. In Figure 13, we show with a red triangle the radio power at 1.4 GHz of the diffuse emission (in terms of integrated radio luminosity νP_ν) versus the maximum power of the CF $P_{\rm CF} = \dot{M}kT/\mu m_{\rm p}$ (here, $\dot{M}$ is the mass accretion rate, k is the Boltzmann constant, T is the global ICM temperature, $\mu \approx 0.61$ is the molecular weight, and m_p is the proton mass) in RBS 797, overlaid onto the values measured for the mini-halo clusters known so far. The monochromatic radio power at the frequency ν is calculated as

$$P_\nu = 4\pi\, D_{\rm L}^2\, S_\nu\, (1+z)^{-(\alpha+1)}, \qquad (3)$$

where $D_{\rm L}$ is the luminosity distance, S_ν is the flux density at the frequency ν, and $(1+z)^{-(\alpha+1)}$ is the K-correction term (Petrosian & Dickey 1973), which in the case of RBS 797 is negligible ($\alpha \sim -1$; Gitti et al. 2006). The radio spectral index α is defined so that $S_\nu \propto \nu^{-\alpha}$. From the flux density measured in Section 3.2, we estimate a radio mini-halo power of $P_{1.4\rm GHz} = (5.2 \pm 0.2) \times 10^{24}$ W Hz^{-1}. From the global cluster temperature derived in Section 4 and the mass accretion rate $\dot{M}$ derived in Section 5, which are measured consistently with the methods adopted for the other objects in Figure 13,[10] we estimate $P_{\rm CF} = 1.55^{+2.12}_{-1.53} \times 10^{44}$ erg s^{-1} (errors at 90% confidence level). Despite its large error bar, we can say that RBS 797 agrees with the observed trend, thus indicating that its diffuse radio emission can be classified as a radio mini-halo.

On the other hand, we stress that the classification of a radio source as a mini-halo is not trivial: their detection is complicated by the fact that the diffuse, low surface brightness emission needs to be separated from the strong radio emission of the central radio galaxy. Furthermore, the criteria adopted to define mini-halos are somewhat arbitrary (e.g., total size, morphology, presence of cool core) and some identifications are still controversial.

7. SUMMARY AND CONCLUSIONS

In this paper, we have shown the results of our analysis of new *Chandra* and VLA observations of the galaxy cluster RBS 797. Both X-ray and radio data reveal a strong interplay between the central radio source and the ICM, suggesting that the cool core cluster RBS 797 is a good candidate to investigate the AGN feedback process. Summarizing our main findings:

1. Our morphological analysis of the deep *Chandra* data confirms the presence of deep, inner X-ray cavities discovered in the previous snapshot observations. Using the surface brightness profile, we estimate the diameters of the cavities to be ∼20 kpc. We also note the presence of edges surrounding the central region of the cluster, which could be the signature of weak shocks that supplement the energy released by the cavity system.
2. We find an enhanced iron abundance in a region that is extended in the direction of the cavities, as predicted by numerical models. This suggests that the AGN outbursts that inflate the cavities also lift metal-enriched gas outward in the direction of the radio jets. Therefore, the AGN in the core contributes to lift the metals with its outburst which drives the cavity inflation. Due to the limited statistics, we are unable to create a metallicity map of the cluster which would be necessary to perform a more detailed study.
3. The power of the cavity system is estimated to be $P_{\rm cav} = 2.5 \times 10^{45}$ erg s^{-1} (Table 3), consistent with the value estimated by Cavagnolo et al. (2011). Comparison to the X-ray luminosity of the gas within the cooling radius ($r_{\rm cool} = 109$ kpc), estimated using deprojected profiles as $L_X = 1.33 \times 10^{45}$ erg s^{-1}, indicates that the mechanical luminosity of the AGN outburst is large enough to balance the radiative losses. The cavity power gives a lower limit on the true power of the AGN, as the possible presence of further cavities and weak shocks would contribute to it, thus providing a more complete estimate of the jet power.
4. We find an indication that the cavities have a higher temperature than the surrounding ICM. Support for this consideration comes both from the projected spectral analysis and from the SR method described in Section 6.2. However, this may only be a projection effect, as we find that the cavities are consistent with being empty of X-ray emitting gas.
5. Our new VLA data detect a 1.4 GHz diffuse radio emission with size comparable to the cooling region (Figure 12). We show how this emission can be classified as a radio mini-halo, following the trend $P_{\rm radio} - P_{\rm CF}$ predicted by the reacceleration model (Section 6.4).

A.D. is a member of the International Max Planck Research School (IMPRS) for Astronomy and Astrophysics at the

[10] In particular, the mass accretion rate is estimated in the framework of the standard cooling flow model (see Gitti et al. 2004, 2007b).

Universities of Bonn and Cologne. A significant part of this work was done by A.D. as a Master student at the University of Bologna. A.D. thanks the Harvard-Smithsonian Center for Astrophysics for the hospitality during the finalization of this work and acknowledges support by the *Chandra* grant GO0-11136X. M.G. acknowledges support by grants ASI-INAF I/023/05/0 and I/088/06/0 and by *Chandra* grants GO0-11003X and GO0-11136X. B.R.M. acknowledges support from the Natural Sciences and Engineering Research Council of Canada.

REFERENCES

Anders, E., & Grevesse, N. 1989, Geochim. Cosmochim. Acta, 53, 197
Bîrzan, L., McNamara, B. R., Nulsen, P. E. J., Carilli, C. L., & Wise, M. W. 2008, ApJ, 686, 859
Bîrzan, L., Rafferty, D. A., McNamara, B. R., Wise, M. W., & Nulsen, P. E. J. 2004, ApJ, 607, 800
Blanton, E. L., Randall, S. W., Clarke, T. E., et al. 2011, ApJ, 737, 99
Blanton, E. L., Randall, S. W., Douglass, E. M., et al. 2009, ApJ, 697, L95
Blanton, E. L., Sarazin, C. L., McNamara, B. R., & Wise, M. W. 2001, ApJ, 558, L15
Böhringer, H., Burwitz, V., Zhang, Y.-Y., Schuecker, P., & Nowak, N. 2005, ApJ, 633, 148
Böhringer, H., Voges, W., Fabian, A. C., Edge, A. C., & Neumann, D. M. 1993, MNRAS, 264, L25
Brüggen, M. 2002, ApJ, 571, L13
Cassano, R., Gitti, M., & Brunetti, G. 2008, A&A, 486, L31
Cavagnolo, K. W., McNamara, B. R., Wise, M. W., et al. 2011, ApJ, 732, 71
Cavaliere, A., & Fusco-Femiano, R. 1976, A&A, 49, 137
Churazov, E., Forman, W., Jones, C., & Böhringer, H. 2000, A&A, 356, 788
Ettori, S., De Grandi, S., & Molendi, S. 2002, A&A, 391, 841
Fabian, A. C. 1994, ARA&A, 32, 277
Fabian, A. C., Sanders, J. S., Ettori, S., et al. 2000, MNRAS, 318, L65
Fabian, A. C., Sanders, J. S., Taylor, G. B., et al. 2006, MNRAS, 366, 417
Fischer, J., Hasinger, G., Schwope, A. D., et al. 1998, Astron. Nachr., 319, 347
Gaspari, M., Brighenti, F., D'Ercole, A., & Melioli, C. 2011a, MNRAS, 415, 1549
Gaspari, M., Melioli, C., Brighenti, F., & D'Ercole, A. 2011b, MNRAS, 411, 349
Giacintucci, S., Markevitch, M., Brunetti, G., Cassano, R., & Venturi, T. 2011, A&A, 525, L10
Giovannini, G., & Feretti, L. 2002, in Merging Processes in Galaxy Clusters, ed. L. Feretti, I. M. Gioia, & G. Giovannini (Astrophysics and Space Science Library, Vol. 272; Dordrecht: Kluwer), 197
Gitti, M., Brighenti, F., & McNamara, B. R. 2012, Adv. Astron., 2012, 1
Gitti, M., Brunetti, G., Feretti, L., & Setti, G. 2004, A&A, 417, 1
Gitti, M., Brunetti, G., & Setti, G. 2002, A&A, 386, 456
Gitti, M., Feretti, L., & Schindler, S. 2006, A&A, 448, 853
Gitti, M., McNamara, B. R., Nulsen, P. E. J., & Wise, M. W. 2007a, ApJ, 660, 1118
Gitti, M., Nulsen, P. E. J., David, L. P., McNamara, B. R., & Wise, M. W. 2011, ApJ, 732, 13
Gitti, M., O'Sullivan, E., Giacintucci, S., et al. 2010, ApJ, 714, 758
Gitti, M., Piffaretti, R., & Schindler, S. 2007b, A&A, 472, 383
Gitti, M., & Schindler, S. 2004, A&A, 427, L9
Kalberla, P. M. W., Burton, W. B., Hartmann, D., et al. 2005, A&A, 440, 775
Keshet, U., & Loeb, A. 2010, ApJ, 722, 737
Kirkpatrick, C. C., Gitti, M., Cavagnolo, K. W., et al. 2009, ApJ, 707, L69
Kirkpatrick, C. C., McNamara, B. R., & Cavagnolo, K. W. 2011, ApJ, 731, L23
Mathews, W. G., & Brighenti, F. 2008, ApJ, 685, 128
Mazzotta, P., Edge, A. C., & Markevitch, M. 2003, ApJ, 596, 190
Mazzotta, P., & Giacintucci, S. 2008, ApJ, 675, L9
McNamara, B. R., & Nulsen, P. E. J. 2007, ARA&A, 45, 117
McNamara, B. R., Nulsen, P. E. J., Wise, M. W., et al. 2005, Nature, 433, 45
McNamara, B. R., Wise, M., Nulsen, P. E. J., et al. 2000, ApJ, 534, L135
Million, E. T., Werner, N., Simionescu, A., et al. 2010, MNRAS, 407, 2046
Nulsen, P. E. J., McNamara, B. R., Wise, M. W., & David, L. P. 2005, ApJ, 628, 629
O'Sullivan, E., Giacintucci, S., David, L. P., et al. 2011, ApJ, 735, 11
Peterson, J. R., & Fabian, A. C. 2006, Phys. Rep., 427, 1
Peterson, J. R., Paerels, F. B. S., Kaastra, J. S., et al. 2001, A&A, 365, L104
Petrosian, V., & Dickey, J. 1973, ApJ, 186, 403
Pfrommer, C., & Enßlin, T. A. 2004, A&A, 413, 17
Rafferty, D. A., McNamara, B. R., Nulsen, P. E. J., & Wise, M. W. 2006, ApJ, 652, 216
Randall, S. W., Forman, W. R., Giacintucci, S., et al. 2011, ApJ, 726, 86
Roediger, E., Brüggen, M., Rebusco, P., Böhringer, H., & Churazov, E. 2007, MNRAS, 375, 15
Salomé, P., & Combes, F. 2003, A&A, 412, 657
Schindler, S., Castillo-Morales, A., De Filippis, E., Schwope, A., & Wambsganss, J. 2001, A&A, 376, L27
Schwope, A., Hasinger, G., Lehmann, I., et al. 2000, Astron. Nachr., 321, 1
Simionescu, A., Roediger, E., Nulsen, P. E. J., et al. 2009a, A&A, 495, 721
Simionescu, A., Werner, N., Böhringer, H., et al. 2009b, A&A, 493, 409
Simionescu, A., Werner, N., Finoguenov, A., Böhringer, H., & Brüggen, M. 2008, A&A, 482, 97
Tamura, T., Kaastra, J. S., Peterson, J. R., et al. 2001, A&A, 365, L87
Vikhlinin, A., Markevitch, M., Murray, S. S., et al. 2005, ApJ, 628, 655
Wise, M. W., McNamara, B. R., Nulsen, P. E. J., Houck, J. C., & David, L. P. 2007, ApJ, 659, 1153
ZuHone, J. A., Markevitch, M., & Lee, D. 2011, ApJ, 743, 16